# Valence-shell photoionization of chlorinelike Ar⁺ ions

A. M. Covington, A. Aguilar,[*] I. R. Covington, G. Hinojosa,[†] C. A. Shirley, and R. A. Phaneuf
*Department of Physics, MS 220, University of Nevada, Reno, Nevada 89557-0058, USA*

I. Álvarez and C. Cisneros
*Instituto de Ciencias Físicas, Universidad Nacional Autónoma de México, Apartado Postal 6-96, Cuernavaca 62131, Morelos, México*

I. Dominguez-Lopez,[‡] M. M. Sant'Anna,[§] and A. S. Schlachter
*Advanced Light Source, Lawrence Berkeley National Laboratory, 1 Cyclotron Road, Berkeley, California 94720, USA*

C. P. Ballance
*Department of Physics, Auburn University, Auburn, Alabama 36840, USA*

B. M. McLaughlin[‖]
*Institute for Theoretical Atomic and Molecular Physics, Harvard Smithsonian Center for Astrophysics, 60 Garden Street,
MS-14, Cambridge, Massachusetts 02138, USA*

Absolute cross-section measurements for valence-shell photoionization of Ar⁺ ions are reported for photon energies ranging from 27.4 to 60.0 eV. The data, taken by merging beams of ions and synchrotron radiation at a photon energy resolution of 10 meV, indicate that the primary ion beam was a statistically weighted mixture of the $^2P^o_{3/2}$ ground state and the $^2P^o_{1/2}$ metastable state of Ar⁺. Photoionization of this Cl-like ion is characterized by multiple Rydberg series of autoionizing resonances superimposed on a direct photoionization continuum. Observed resonance line shapes indicate interference between indirect and direct photoionization channels. Resonance features are spectroscopically assigned and their energies and quantum defects are tabulated. The measurements are satisfactorily reproduced by theoretical calculations based on an intermediate coupling semirelativistic Breit-Pauli approximation.

PACS number(s): 32.80.Fb, 32.80.Zb, 32.80.Ee

## I. INTRODUCTION

Photoionization (PI) of ions is a fundamental process of importance in many high-temperature plasma environments, such as those occurring in stars and nebulae [1] and in inertial-confinement fusion experiments [2]. Quantitative measurements of photoionization cross sections for ions provide precision data on ionic structure and guidance to the development of theoretical models of multielectron interactions. In addition, the opacity databases [3–5] that are critical to the modeling and diagnostics of hot, dense plasmas consist almost entirely of theoretical calculations performed in $LS$ coupling. High-resolution absolute photoionization cross-section measurements are therefore necessary to benchmark the validity of these term-resolved data.

Due to the shortcomings of solar studies, abundance determinations shed more light on argon abundance at near-solar metallicity. Such an approach has been suggested by recent studies on a similar case of neon in B-type stars in the Orion nebula [6,7] and in the interstellar medium (ISM) toward the Crab nebulae [8]. Photoionization cross-section data on this Cl-like ion are required to accurately determine elemental abundances, for example, in the whole stellar sample of B-type stars where the $\lambda = 442.6$ nm and $\lambda = 443.0$ nm lines of Ar⁺ are vividly seen in the B main-sequence stars of the Orion nebulae [9]. The non-local-thermodynamic-equilibrium (non-LTE) abundance calculations were based on photoionization cross-section data taken from the Opacity Project [3] calculated in $LS$ coupling. It has been shown for a variety of ions, that the Opacity Project data have severe limitations when compared to high-resolution experimental data [10,11].

Photoionization phenomena are bound-free processes characterized by interfering channels. In the direct photoionization of a positive ion, the cross section rises from zero as a step function at the ionization threshold energy and falls off monotonically with increasing photon energy. This process leads immediately to the production of Ar²⁺ and a free electron

$$\begin{array}{ccc} & (Ar^+)^{**} & \\ & \nearrow \qquad \searrow & \\ \gamma + Ar^+ & \longrightarrow & Ar^{2+} + e^-. \end{array} \qquad (1)$$
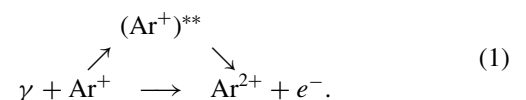
---
[*]Present address: Advanced Light Source, Lawrence Berkeley National Laboratory, 1 Cyclotron Road, MS 7-100, Berkeley, California 94720, USA.

[†]Present address: Instituto de Ciencias Físicas, Universidad Nacional Autónoma de México, Apartado Postal 6-96, Cuernavaca 62131, Morelos, México.

[‡]Present address: Centro Nacional de Metrología, Querétaro, Qro. 76900, México.

[§]Present address: Instituto de Física, Universidade Federal do Rio de Janeiro, Caixa Postal 68528, 21945-970 Rio de Janeiro RJ, Brazil.

[‖]Present address: Centre for Theoretical Atomic, Molecular and Optical Physics (CTAMOP), School of Mathematics and Physics, The David Bates Building, 7 College Park, Queen's University of Belfast, Belfast BT7 1NN, United Kingdom.

Superimposed upon this direct photoionization cross section are a series of resonances occurring at discrete photon energies corresponding to the excitation of autoionizing states in the singly charged $Ar^+$ ion. Interference between the indirect and direct photoionization channels produces characteristic Fano-Beutler line profiles for the resonances [12], providing further insight into the electronic structure of the ion and the dynamics of the photoionization process.

A thorough compilation of merged-beams photoionization studies has been presented in a topical review by Kjeldsen [13] and a previous review by West [14]. The technique of photoion-yield spectroscopy using synchrotron radiation was pioneered by Lyon and collaborators [15] at the Daresbury synchrotron in the UK, and involves merging ion beams accelerated to keV energies with monochromatic, tunable beams of synchrotron radiation. Photoions produced by their interaction over common paths of tens of centimeters may be magnetically or electrostatically separated from the parent ion beam. The directed ion beam and negligible momentum transfer permit a complete collection of the photoions. If the energy of the ion beam is not too high and ultra-high vacuum conditions prevail, the background produced by stripping collisions of the primary ion beam with residual gas is manageable, and may be subtracted by chopping the photon beam. The merged-beams technique is particularly amenable to absolute cross-section measurements [16].

Until recently, because of the relatively low density presented by a space-charge-limited ion beam ($\sim 10^6$ cm$^{-3}$), data for ions were limited mainly to singly-charged alkali, alkaline earth, and transition metal ions with large photoionization cross sections [14]. The advent of third-generation synchrotron radiation sources (3GLS) with insertion devices increased the photon beam intensities available to experimenters by nearly three orders of magnitude, making possible the study of photoionization of ions with unprecedented sensitivity and spectral resolution. This has permitted measurements with ions of the lighter and more astrophysically abundant elements, e.g., $C^+$ [17], $O^+$ [18,19], $C^{2+}$ [20], and more recently $C^{3+}$ [21] and $N^{3+}$ and $O^{4+}$ [22], which are helping to refine theoretical descriptions of the photoionization process.

As previously indicated, the properties of argon ions are of importance in atmospheric and astrophysical plasmas and are widely used in laboratory plasmas as diagnostic impurities [23,24]. Properties of argon ions also find many applications in plasma etching and lasers [25]. In the present study, high-resolution absolute photoionization cross-section measurements and theoretical calculations are presented for the $Ar^+$ ion at photon energies ranging from the photoionization threshold to 60 eV.

## II. EXPERIMENT

The experiment was conducted on undulator beamline 10.0.1.2 of the Advanced Light Source (ALS) at Lawrence Berkeley National Laboratory. The ion-photon-beam (IPB) end station is based on the merged-beams technique and photoion spectroscopy using tunable synchrotron radiation. The apparatus and methodology were described in detail previously for measurements of photoionization cross sections for $Ne^+$ ions [10]. Initial measurements of photoionization

cross sections for $O^+$ ions [18] and $C^{2+}$ ions [20] using the IPB end station were reported in the literature. The ALS group has recently reported detailed experimental and theoretical studies on the Cl-like calcium ($Ca^{3+}$) ion [26] in addition to a variety of other singly and multiply charged ions, particularly of astrophysical interest, using this same IPB end station: He-like; $Li^+$ [27,28], Li-like; $B^{2+}$ [29], Be-like; $C^{2+}$ [30], $B^+$ [31], $C^{2+}$, $N^{3+}$, and $O^{4+}$ [22,32], B-like; $C^+$ [33], F-like; $Ne^+$ [10], N-like ions; $O^+$ [18], $F^{2+}$ and $Ne^{3+}$ [11]. These high-resolution experimental results enable theoretical studies to be benchmarked, so that the resulting data can be used with confidence in various astrophysical applications that utilize modeling codes such as CLOUDY [34,35] and XSTAR [36].

### A. Photon beam

The photon beam was produced by a 10-cm period undulator installed in the 1.9 GeV electron storage ring to serve ALS beamline 10.0.1. A grazing-incidence spherical-grating monochromator delivered a highly collimated photon beam of spatial width less than 1 mm and divergence less than 0.5°. The beamline produces a photon flux of $5 \times 10^{12}$ photons per second in a bandwidth of 0.01% at an energy of 40 eV and three gratings cover the energy range 17–340 eV. Spectral resolving powers $E/\Delta E$ as high as 40 000 are available at reduced photon flux. All of the measurements with $Ar^+$ ions were carried out with a gold-surfaced spherical grating ruled at 380 lines/mm. The photon energy was scanned by rotating the grating and translating the exit slit of the monochromator while simultaneously adjusting the undulator gap to maximize the beam intensity. The spectral resolution was preselected by adjusting the entrance and exit slits of the monochromator. The photon flux was measured by an absolutely calibrated silicon x-ray photodiode, and was typically $(2–3) \times 10^{13}$ photons/s at a nominal spectral resolving power of 2 000. The analog output from a precision current meter was directed to a voltage-to-frequency converter, which provided a normalization signal to a personal-computer-based data acquisition system. The photon beam was time modulated (mechanically chopped) at 0.5 Hz using a stepping-motor controlled paddle to separate photoions from background produced by stripping of the parent ion beam on residual gas in the ultra-high vacuum system. The photon energy scale was calibrated using measurements [18] of the well-known $O^+$ ground-state ($^4S$) and metastable-state ($^2P$ and $^2D$) energy thresholds, allowing for the Doppler shift due to the ion motion in the laboratory frame. The absolute uncertainty in the photon energy scale is estimated to be $\pm 10$ meV.

### B. Ion beam

The $^{40}Ar^+$ ions were produced by the Cuernavaca Ion Gun Apparatus (CIGA) in a hot-filament, low-pressure discharge-type ion source, and accelerated to an energy of 6 keV. The ion beam was focused by a series of cylindrical electrostatic einzel lenses and the $Ar^+$ ion beam selected by a 60° analyzing magnet with a mass resolving power of 100. The ion beam trajectory and its cross-sectional area were defined by adjustable horizontal and vertical beam slits located downstream of the analyzing magnet. The collimated $Ar^+$ beam was typically

a few mm in diameter, with a current in the range of 500–650 nA. Three stages of differential pumping with turbomolecular pumps and a cryopump assured a downstream vacuum in the $10^{-10}$ torr range with beams present.

### C. Merger and beam interaction region

A pair of $90°$ spherical-sector bending plates merged the ion beam onto the axis of the counterpropagating photon beam. Fine-tuning of the overlap of the beams was achieved with two sets of mutually perpendicular electrostatic steering plates mounted immediately before the merger plates. A cylindrical einzel lens focused the beam in the center of the interaction region, which consisted of an isolated stainless-steel-mesh cylinder to which an electric potential (typically + 2 kV) was applied, thereby energy-labeling photoions produced in this region. Series of entrance and exit apertures accurately defined the effective length (29.4 cm) of the interaction region. Two-dimensional intensity distributions of both beams were measured by commercial rotating-wire beam profile monitors installed just upstream and downstream of the interaction region, and by a translating-slit scanner located in the middle of the region. The profile monitors permitted the positions and spatial profiles of the two beams to be continuously monitored on an oscilloscope while tuning the beams. Two 500 l/s mag-ion pumps assured ultra-high vacuum conditions in this region when the photon and ion beams were present.

### D. Demerger and ion charge analyzer

A $45°$ dipole analyzing magnet located downstream of the interaction region demerged the beams and separated the $Ar^{2+}$ products from the parent $Ar^+$ beam, which was collected in an extended Faraday cup. The magnetic field was set such that the $Ar^{2+}$ product ions passed through an aperture in the back of the Faraday cup. A spherical $90°$ electrostatic deflector directed them onto a stainless-steel plate biased at $-550$ V, from which secondary electrons were accelerated and detected by a microsphere-plate electron multiplier used in a pulse-counting mode. The deflection planes of the demerger magnet and this spherical deflector were orthogonal, permitting the $Ar^{2+}$ products to be swept across the detector in mutually perpendicular directions, providing a diagnostic of their complete collection. To this end, a cylindrical einzel lens located downstream of the interaction region provided a further diagnostic, but was found to be unnecessary and was turned off during the measurements. The absolute efficiency of the photoion detector was calibrated *in situ* using an averaging subfemtoampere meter to record the $Ar^{2+}$ photoion current, which was then compared to the measured photoion count rate. The primary $Ar^+$ ion beam current was measured by a precision current meter, whose analog output was directed to a voltage-to-frequency converter, providing a normalization signal to the data acquisition system.

## III. THEORY

For comparison with high-resolution measurements such as those at ALS, state-of-the-art theoretical methods are required using highly correlated wave functions. In addition, relativistic effects are required, since fine-structure effects can be re-

solved. As metastable states are populated in the $Ar^+$ ion beam, additional theoretical calculations were required to assist in the determination of their fraction. Similar features have previously been demonstrated by past detailed experimental and theoretical photoionization studies on a number of simple and complex ions, as outlined in Sec. II.

Previous photoionization cross-section calculations for $Ar^+$ were carried out in $LS$ coupling for the Opacity Project [3]. To provide a benchmark comparison and a guide to the experiment, photoionization cross-section calculations were performed in intermediate coupling (Breit-Pauli) using the $R$-matrix method [37]. The inclusion of relativistic effects is necessary due to the high energy resolution of the measurements (nominally 10 meV). This theoretical approach optimizes use of limited experimental beam time, since coarse energy scans may be used in resonance-free regions and fine scans at high resolution may be concentrated in energy ranges where dense resonance structure is predicted. In the theoretical work, 24 $LS$ terms of the product $Ar^{2+}$ ion were used, arising from the configurations $1s^22s^22p^63s3p^4$, $1s^22s^22p^63s3p^5$, $1s^22s^22p^63s^23p^23d^2$, and $1s^22s^22p^63p^6$. The high-resolution spectral scan measurements show resonance peaks with an energy separation of magnitude comparable to the fine-structure splitting of the $1s^22s^22p^63s^23p^5\,^2P^o_{3/2,1/2}$ levels of $Ar^+$.

In the semirelativistic $R$-matrix calculations performed for this complex, the 24 $LS$ terms give rise to 48 $LSJ$ levels for the product $Ar^{2+}$ ion core, all of which were included in the close-coupling photoionization cross-section calculations. For the $Ar^{2+}$ product ion the orbital basis set used to describe the 24 target $LS$ terms was limited to $n=3$ in constructing the multiconfiguration interaction wave functions used in the calculations. Photoionization cross sections were determined for both the $^2P^o_{3/2}$ ground and the metastable $^2P^o_{1/2}$ initial states of the $Ar^+$ ion due to the population of metastable states in the primary ion beam used in the measurements.

An efficient parallel version [38] of the $R$-matrix programs [39–41] was used to determine all the photoionization cross sections. The scattering wave functions were generated by allowing for triple-electron promotions out of the base configuration $3s^23p^5$ of $Ar^+$ into the $n=3$ orbital set employed for the photoionization cross sections for both the ground $^2P^o_{3/2}$ and the metastable $^2P^o_{1/2}$ initial states of $Ar^+$ in intermediate coupling ($LSJ$).

All the scattering calculations were performed with 20 continuum basis functions and a boundary radius of 7.0 Bohr radii. In the case of the $^2P^o_{3/2}$ initial ground state, the dipole selection rule requires the dipole transition matrices $3/2^o \rightarrow 1/2^e, 3/2^e, 5/2^e$ to be calculated, whereas for the metastable $^2P^o_{1/2}$ initial state, only the dipole matrices for the transitions $1/2^o \rightarrow 1/2^e, 3/2^e$ are required. The Hamiltonian matrices for the $1/2^o$, $3/2^o$, $5/2^e$, $3/2^e$, and $1/2^e$ symmetries were calculated over the entire range of $LS$ partial waves that contribute to these $J\pi$ symmetries. The $Ar^{2+}$ theoretical energies were shifted to experimental values in the diagonalization procedure of the appropriate Hamiltonians so that the energy positions of resonances relative to each ionization threshold would be improved [42,43]. This energy shift was less than 1% for all the energy levels involved. For both

the $^2P^o_{3/2}$ ground and the metastable $^2P^o_{1/2}$ initial states, the electron-ion collision problem in the outer region was then solved with the parallel $R$-matrix codes using a fine energy mesh of 0.68 $\mu$eV ($5 \times 10^{-8}$ Rydbergs). This ensured that the fine resonance structure in the respective photoionization cross sections was fully resolved, particularly in the near-threshold energy region. The absolute theoretical photoionization cross sections were convoluted with a Gaussian with a full width at half maximum (FWHM) corresponding to the experimental resolution (nominally 10 meV) and statistically weighted in order to compare directly with the experimental data.

The multichannel $R$-matrix QB technique (applicable to atomic [44,45] and molecular complexes [46] which defines matrices $Q$ and $B$ in terms of asymptotic solutions, the $R$-matrix and energy derivatives) was used to determine the resonance parameters. In the QB method, the resonance width $\Gamma$ is determined from the inverse of the energy derivative of the eigenphase sum $\delta$ at the position of the resonance energy $E_r$ via

$$\Gamma = 2 \left[ \frac{d\delta}{dE} \right]^{-1}_{E=E_r} = 2[\delta']^{-1}_{E=E_r}. \tag{2}$$

This approach exploits the analytical properties of the $R$ matrix to obtain the energy derivative of the reactance (**K**) matrix and has previously proved very successful in locating fine resonance features in the cross sections for multichannel electron scattering.

## IV. RESULTS

### A. Absolute cross-section measurements

Absolute measurements of photoionization cross sections were performed at a number of discrete photon energies where there are no resonant features in the photoion-yield spectrum. At each such photon energy ($h\nu$), the value of the total absolute photoionization cross section $\sigma_{PI}$ in cm$^2$ was determined from experimentally measured parameters:

$$\sigma_{PI}(h\nu) = \frac{R \, q \, e^2 \, v_i \, \epsilon}{I^+ I^\gamma \, \Omega \, \delta_1 \, \Delta \int F(z) dz}, \tag{3}$$

where $R$ is the photoion count rate (s$^{-1}$), $q$ is the charge state of the parent ion, $e = 1.60 \times 10^{-19}$ C, $v_i$ is the ion beam velocity (cm/s), $\epsilon$ is the responsivity of the photodiode (electrons/photon), $I^+$ is the ion beam current (A), $I^\gamma$ is the photodiode current (A), $\Omega$ is the photoion collection efficiency, $\delta_1$ is the pulse transmission fraction of the photoion detection electronics (determined by the pulse-discriminator setting), $\Delta$ is the measured absolute photoion detection efficiency, and the beam overlap integral $\int F(z) dz$ defines the spatial overlap of the photon and ion beams along the common interaction path in units of cm$^{-1}$. The propagation direction of the ion beam is defined as the $z$ axis. At each of the three positions $z_i$ at which beam intensity profiles were measured, the form factor $F(z_i)$ was determined by the following relation:

$$F(z_i) = \frac{\int \int I^+(x,y) I^\gamma(x,y) \, dx \, dy}{\int \int I^+(x,y) \, dx \, dy \int \int I^\gamma(x,y) \, dx \, dy}. \tag{4}$$

The absolute photoion detection efficiency was determined *in situ* by comparing the count rate of Ar$^{2+}$ ions on the

TABLE I. Values of experimental parameters for a typical Ar$^+$ absolute photoionization cross-section measurement at 32.5 eV.

| Parameter | Value(s) |
|---|---|
| Ion beam energy | 6.0 keV |
| Ion beam current, $I^+$ | 620.0 nA |
| Photon energy, $h\nu$ | 32.4 eV |
| Photodiode current, $I^\gamma$ | 19.7 $\mu$A |
| Photon flux | $5.6 \times 10^{13}$ photons/s |
| Interaction bias voltage, $V_{int}$ | + 2.0 kV |
| Ion interaction velocity, $v_i$ | $1.39 \times 10^7$ cm/s |
| Ar$^{2+}$ signal rate, $R$ | 7012.5 s$^{-1}$ |
| Ar$^{2+}$ background rate | 45.2 s$^{-1}$ |
| Form Factors: $F(z_1)$, $F(z_2)$, $F(z_3)$ | 41.22, 28.22, 19.17 cm$^{-2}$ |
| Photodiode responsivity, $\epsilon$ | 7.81 electrons/photon |
| Merge-path length, $L$ | 29.4 cm |
| Pulse transmission fraction, $\delta_1$ | 0.75 |
| Photoion collection efficiency, $\Omega$ | 1.00 |
| Photoion detection efficiency, $\Delta$ | 0.216 |
| Cross section, $\sigma$ | 10.95 Mb |
| | (1 Mb = $10^{-18}$ cm$^2$) |

detector with the current measured using a calibrated averaging subfemtoammeter. In Table I, experimental parameters are given for a typical absolute cross-section measurement at a photon energy of 32.5 eV. Such measurements were repeated several times at each photon energy.

Table II presents the relative, absolute, and the total uncertainties (their quadrature sums) in the photoionization cross-section measurements estimated at 90% confidence level (two standard deviations on statistical uncertainties) or at an equivalent confidence level for systematic uncertainties. Table III presents the absolute photoionization cross-section values that were determined at the selected photon energies. The data from Table III are plotted in Fig. 1 with error bars representing the total uncertainties. Photon energy scans taken over the energy range 27.4–60 eV at a resolution of 10 meV with 1.5-meV steps were normalized to these absolute measurements by fitting a polynomial to their measured ratio as a function of photon energy. These data are presented in Fig. 1 as small triangles.

TABLE II. Systematic uncertainties in absolute cross-section measurements estimated at 90% confidence level.

| Source | Relative | Absolute | Total |
|---|---|---|---|
| Counting statistics | 2% | | 2% |
| Photoion detector efficiency | | 10% | 10% |
| Photoion collection efficiency | 2% | 2% | 3% |
| Pulse counting efficiency | | 3% | 3% |
| Primary ion collection efficiency | | 2% | 2% |
| Ion current measurement | | 2% | 2% |
| Photodiode responsivity | 5% | 10% | 11% |
| Photodiode current measurement | 2% | 2% | 3% |
| Beam profile measurement | 3% | 7% | 8% |
| Beam overlap integral | 10% | 7% | 12% |
| Interaction length | | 2% | 2% |
| Quadrature sum | 12% | 18% | 22% |

TABLE III. Measured values of the total absolute cross sections for photoionization of Ar$^+$.

| Energy (eV) | Cross section ($10^{-18}$ cm$^2$) | Total uncertainty ($10^{-18}$ cm$^2$) |
|---|---|---|
| 29.5 | 21.4 | 4.6 |
| 32.5 | 11.6 | 2.5 |
| 36.0 | 6.0 | 1.3 |
| 42.0 | 1.2 | 0.3 |
| 47.0 | 0.9 | 0.2 |
| 49.0 | 1.0 | 0.2 |
| 56.0 | 1.3 | 0.3 |
| 59.0 | 1.4 | 0.3 |

Figure 2 presents the ALS measured photoionization cross section in the region of the $^2P_{3/2}$ ground-state and $^2P_{1/2}$ metastable-state ionization threshold energies at 27.630 and 27.452 eV, respectively, according to those given by the NIST tabulations [42]. The ratio of the magnitudes of the two threshold cross-section steps is $2.06 \pm 0.10$, consistent with a statistical population (proportional to $2J + 1$) of ground- and metastable-state ions in the primary ion beam. The present measurements are therefore considered to correspond to a sum of the $^2P_{3/2}$ ground-state cross section multiplied by 2/3 and the metastable-state $^2P_{1/2}$ cross section multiplied by 1/3. The presence of the metastable component adds complexity to the observed resonance structure and to its interpretation. A very small offset of the measured cross section from zero below the $^2P_{1/2}$ threshold is attributed to the presence of higher-order radiation from the undulator, which is dispersed by the grating and estimated to comprise 6% of the total photon flux in this energy region. In this threshold region, a detailed comparison
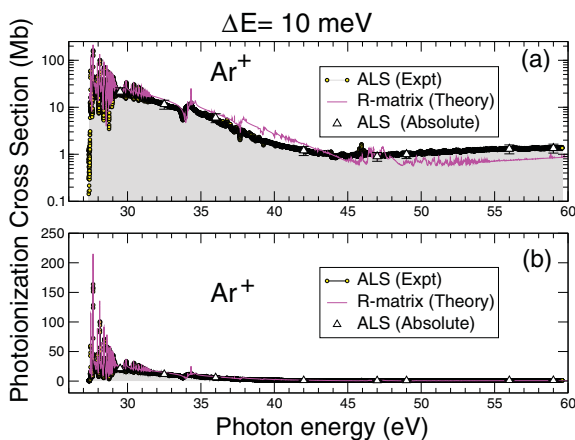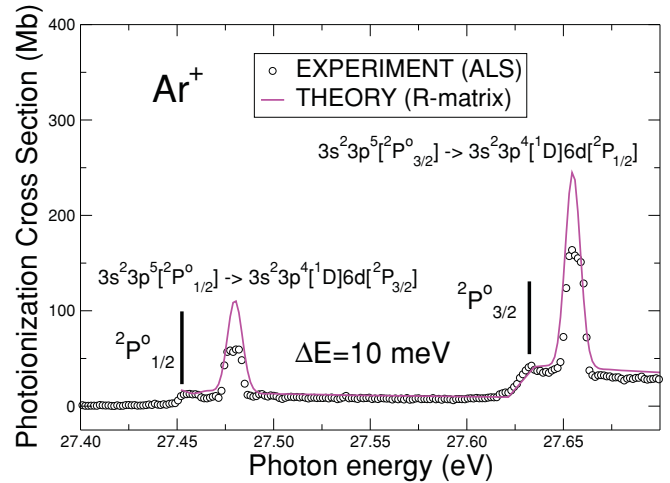


FIG. 2. (Color online) High-resolution PI cross-section measurements from the ALS at 10-meV energy resolution in the photon energy region of the $^2P_{3/2}$ ground-state and $^2P_{1/2}$ metastable-state ionization thresholds of Ar$^+$ at 27.630 and 27.452 eV, respectively. The small, nonzero cross section at energies below both thresholds is attributed to higher-order radiation in the photon beam. Theoretical results are from an intermediate coupling Breit-Pauli $R$-matrix calculation, statistically weighted for the ground and metastable state. The theoretical results have been convoluted with a Gaussian of 10 meV FWHM to simulate the photon energy bandwidth of the experiment.

of the ALS experimental results with theoretical results (from a Breit-Pauli calculation performed in intermediate coupling) show excellent agreement. In order to make a direct comparison with experiment in this energy region, the theoretical results were convoluted with a FWHM Gaussian
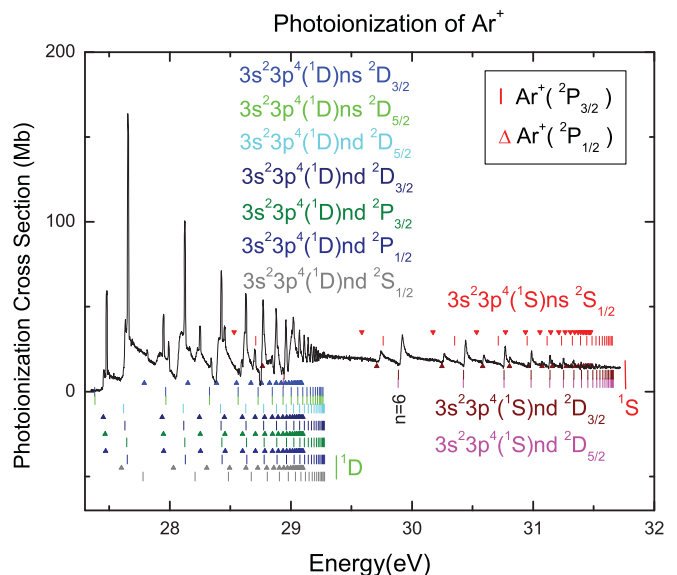


FIG. 1. (Color online) Overview of experimental cross-section measurements and theory for Ar$^+$ (shaded area) at a resolution of 10 meV over an energy range from the ionization threshold to 60 eV; (a) cross sections on a logarithmic scale, (b) cross section on a linear scale. The absolute cross-section measurements are indicated by open triangles with error bars. The curve represents a 48-level close-coupling Breit-Pauli $R$-matrix calculation performed in intermediate coupling. For comparison, the theory curve is a statistically weighted sum of cross sections for photoionization from the ground and metastable states and has been convoluted with a FWHM Gaussian of 10 meV.



FIG. 3. (Color online) Experimental results from the ALS for the PI cross sections of Ar$^+$ for photon energies ranging from 27 to 32 eV with a photon energy resolution of 10 meV. The members of Rydberg series of resonances originating from the $^2P^o_{1/2}$ metastable (|) and $^2P^o_{3/2}$ ground states ($\triangle$) of Ar$^+$ are identified. The resonance assignments were determined from the NIST tabulated levels for Ar II and Ar III [42].
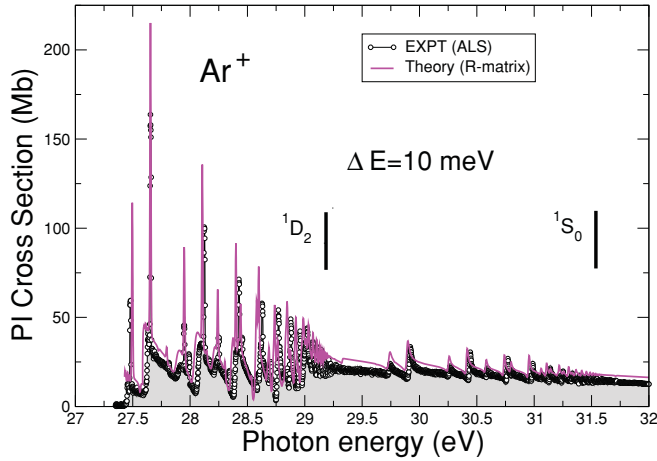
FIG. 4. (Color online) Experimental results from the ALS for the PI cross sections of $Ar^+$ for photon energies ranging from 27 to 32 eV with a photon energy resolution of 10 meV compared with theoretical results from a 48-state Breit-Pauli $R$-matrix calculation. The theoretical results have been convoluted with a Gaussian of FWHM of 10 meV and statistically averaged over the ground and metastable states.

of 10 meV and statistically weighted over the ground and metastable states. The two strong resonance features observed in the threshold energy region of the ALS photoionization experimental measurements (located at 27.481 and 27.658 eV, respectively; see Fig. 2) resulting in photoexcitation of the $3s^2 3p^4 (^1D_2) 6d$ Auger state (from either the ground state or metastable states of $Ar^+$), are reproduced suitably well by the present theoretical Breit-Pauli calculations performed in intermediate coupling.

The peak heights of the stronger calculated resonances exceed the measured values, and the experimental line shapes of the resonances at 27.48 and 27.66 eV are non-Gaussian. This
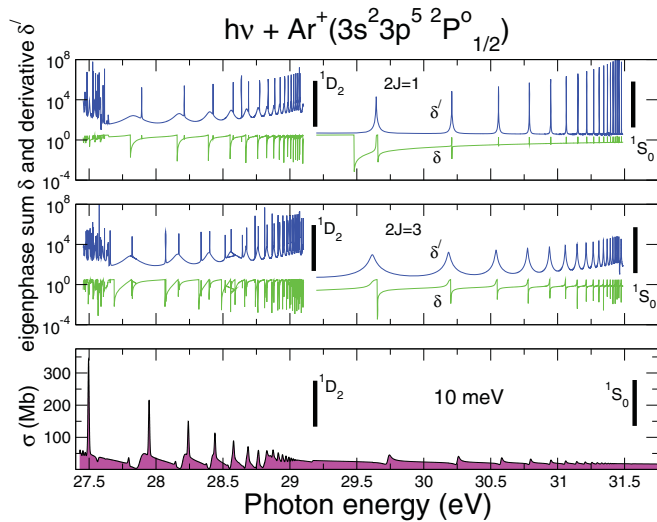


FIG. 6. (Color online) Linewidths (meV) for the dominant $3s^2 3p^4 (^1D_2) ns, nd$ resonance series converging to the $^1D_2$ threshold of the product $Ar^{2+}$ ion originating from the initial $Ar^+ (^2P^o_{1/2})$ metastable state. The $3s^2 3p^4 (^1D_2) ng$ Rydberg resonance series have linewidths very much less than $10^{-2}$ meV and have not been analyzed.

suggests a possible saturation effect due to the dead time of the photoion counting system at the higher signal counting rates. The measured ratios of the strengths of these two resonances further suggest that the ground-state fraction in the primary ion beam may have been closer to 0.73 than the value of 0.67 based on statistical weights that was used to scale the theoretical results for comparison with experiment.

In Fig. 3 we present the experimental data taken at 10 meV in the photon energy region from threshold to approximately 32 eV. As can been seen from Fig. 3, there is extremely rich resonance structure evident in photoionization cross-section data. The assignments of the various Rydberg resonance series



FIG. 5. (Color online) Eigenphase sum $\delta$ and its derivative $\delta'$ for each $2J^\pi$ contributing to the total PI cross section $\sigma$ originating from the initial $Ar^+ (^2P^o_{1/2})$ metastable state. The PI cross section has been convoluted with a FWHM Gaussian of 10 meV to simulate the photon experimental bandwidth.
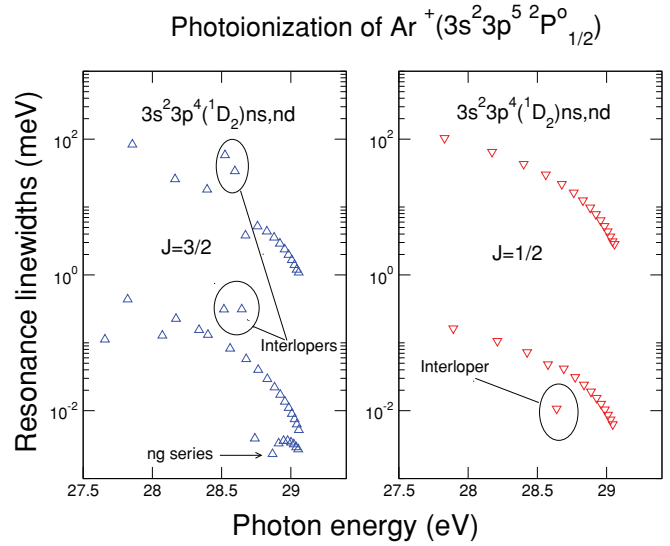


FIG. 7. (Color online) Linewidths (meV) for the dominant $3s^2 3p^4 (^1S_0) ns, nd$ resonance series converging to the $^1S_0$ threshold of the product $Ar^{2+}$ ion originating from the initial $Ar^+ (^2P^o_{1/2})$ metastable state.

FIG. 8. (Color online) Eigenphase sum $\delta$ and its derivative $\delta'$ for each $2J^\pi$ contributing to the total PI cross section $\sigma$ originating from the initial $Ar^+(^2P^o_{3/2})$ ground state. The PI cross section has been convoluted with a FWHM Gaussian of 10 meV to simulate the photon experimental bandwidth.
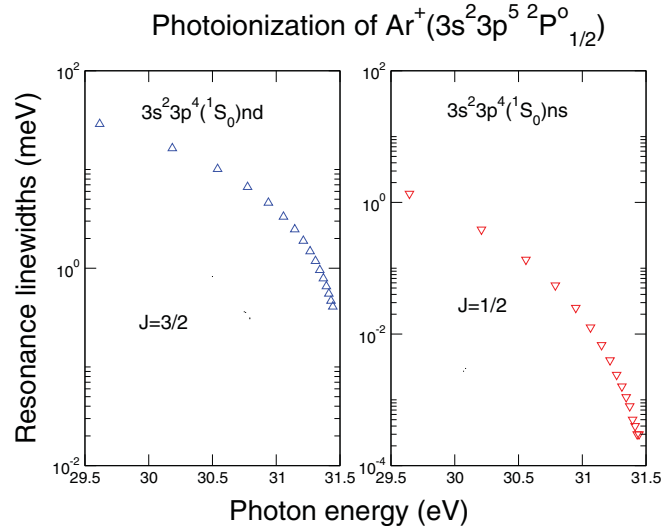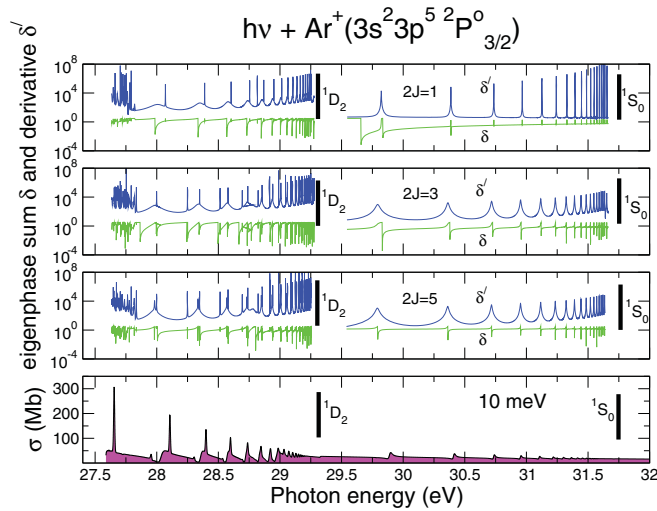


FIG. 10. (Color online) Linewidths (meV) for the dominant $3s^23p^4(^1S_0)ns,nd$ resonances series converging to the $^1S_0$ threshold of the product $Ar^{2+}$ ion originating from photoionization of the initial $Ar^+(^2P^o_{3/2})$ ground state.

are given based on the NIST tabulated levels for Ar II and Ar III [42]. Only the prominent resonance series are analyzed in detail. Figure 4 illustrates the same energy range but includes the comparison with the theoretical results obtained from the intermediate-coupling Breit-Pauli calculations. Here again theory has been convoluted with a FWHM Gaussian of 10 meV and statistically weighted over the ground and metastable states to make a direct comparison with experiment in this energy region. Once again it is seen there is remarkable agreement between theory and experiment, both on the absolute cross-section scale and on the photon energy scale.
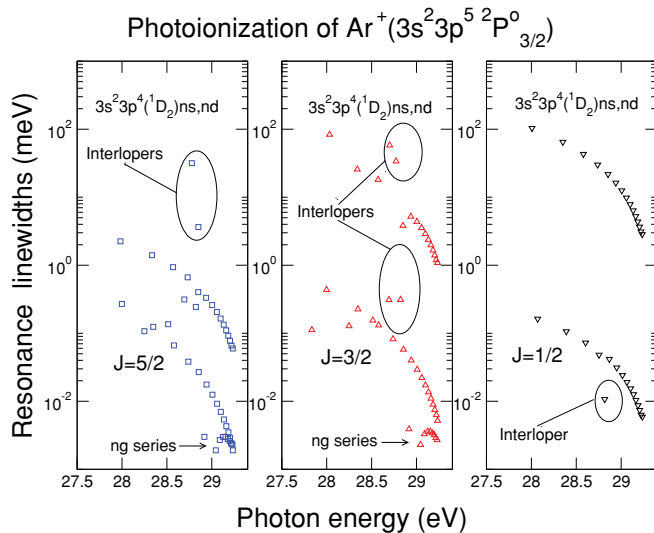
## B. Resonances

In the photon energy range 27–32 eV, a wealth of resonance structure is observed in the PI cross sections as illustrated in Fig. 3. We note that below the $^1D_2$ threshold of the product $Ar^{2+}$ ion, $3s^23p^4(^1D_2)\,ns\,^2D_{3/2,5/2}$, $3s^23p^4(^1D_2)nd\,^2D_{3/2,5/2}$, $3s^23p^4(^1D_2)nd\,^2P_{1/2,3/2}$, and $3s^23p^4(^1D_2)nd\,^2S_{1/2}$ dominant Rydberg resonance series may occur from the angular momentum coupling rules.

At higher photon energies, $3s^23p^4(^1S_0)nd\,^2D_{3/2,5/2}$ and $3s^23p^4(^1S_0)ns\,^2S_{1/2}$ Rydberg resonance series converging to the $^1S_0$ threshold of the corresponding product $Ar^{2+}$ ion are observed. The resonance series found are illustrated in Figs. 5–10. For resonances converging to both the $^1D_2$ and $^1S_0$ thresholds of the $Ar^{2+}$ ion, only the dominant resonance series are analyzed.

To assist in the identification of the dominant resonance features observed in the photoionization spectra, a theoretical analysis was carried out based on the widely used QB technique for determining resonance parameters in atomic and molecular systems [44–46]. This technique exploits the properties of the $R$ matrix in multichannel scattering and is particularly helpful for locating and determining the properties of narrow resonances found in the spectra.

The relationship between the principal quantum number $n$, the effective quantum number $\nu$, and the quantum defect $\mu$ for an ion of effective charge $\mathcal{Z}$ is given by $\nu = n - \mu$, where the resonance position $\epsilon_r$ can be determined from Rydberg's formula

$$\epsilon_r = \epsilon_\infty - \mathcal{Z}^2/\nu^2, \tag{5}$$

where $\epsilon_\infty$ is the resonance series limit.

Prominent Rydberg resonance series observed in the experimental photoionization spectra have been analyzed and assigned according to their quantum defects. The NIST tabulations were used as a helpful guide in the assignment. The principal quantum number $n$, resonance energy in eV,



FIG. 9. (Color online) Linewidths (meV) for the dominant $3s^23p^4(^1D_2)ns,nd$ resonances series converging to the $^1D_2$ threshold of the product $Ar^{2+}$ ion originating from photoionization of the initial $Ar^+(^2P^o_{3/2})$ ground state. The $3s^23p^4(^1D_2)ng$ Rydberg resonance series have linewidths very much less than $10^{-2}$ meV and have not been analyzed.
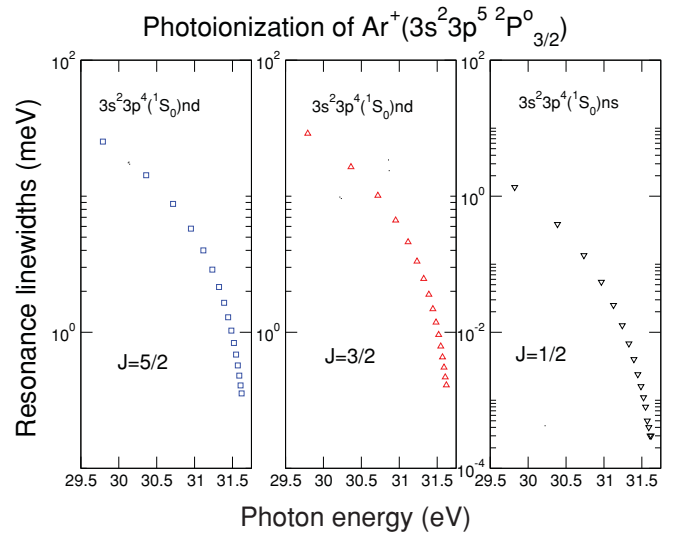
TABLE IV. Principal quantum numbers $n$, resonance energies (eV), quantum defects $\mu$, and autoionization linewidths [$\Gamma$ (meV)], determined by the QB method for the dominant $3s^23p^4(^1S_0)ns,nd$ series observed in the photoionization spectra originating from the $3s^23p^5\,^2P^o_{1/2}$ metastable state of Ar$^+$.

| Initial state | $n$ | Rydberg series $3s^23p^4(^1D_2)ns,nd$ Energy (eV) | $\mu$ | Width ($\Gamma$) $3s^23p^4(^1D_2)ns,nd$ Energy(meV) | Rydberg series $3s^23p^4(^1S_0)ns,nd$ Energy (eV) | $\mu$ | Width ($\Gamma$) $3s^23p^4(^1S_0)ns,nd$ Energy (meV) |
|---|---|---|---|---|---|---|---|
| | | | | $j=1/2$ | | | |
| $3s^23p^5\,^2P^o_{1/2}$ | [7s] | | | | 29.645 | 1.692 | 1.36 |
| | 8 | 27.830 | 1.673 | 103.4 | 30.209 | 1.691 | 0.39 |
| | 9 | 28.173 | 1.682 | 64.8 | 30.558 | 1.690 | 0.14 |
| | 10 | 28.401 | 1.688 | 43.0 | 30.789 | 1.689 | 0.06 |
| | 11 | 28.561 | 1.692 | 30.0 | 30.949 | 1.688 | 0.03 |
| | 12 | 28.677 | 1.695 | 21.8 | 31.065 | 1.688 | 0.01 |
| | 13 | 28.763 | 1.698 | 16.3 | 31.151 | 1.688 | $<10^{-2}$ |
| | 14 | 28.829 | 1.699 | 12.5 | 31.217 | 1.688 | $<10^{-2}$ |
| | 15 | 28.881 | 1.701 | 9.8 | 31.269 | 1.688 | $<10^{-2}$ |
| | 16 | 28.923 | 1.702 | 7.8 | 31.311 | 1.687 | $<10^{-2}$ |
| | … | | | | | | |
| | $\infty$ | 29.189 | | | 31.596 | | |
| | | | | $j=1/2$ | | | |
| $3s^23p^5\,^2P^o_{1/2}$ | [6d] | | | | | | |
| | 7 | 27.830 | 0.521 | 0.16 | | | |
| | 8 | 28.211 | 0.540 | 0.11 | | | |
| | 9 | 28.426 | 0.554 | 0.07 | | | |
| | 10 | 28.576 | 0.574 | 0.05 | | | |
| | 11 | 28.691 | 0.546 | 0.04 | | | |
| | 12 | 28.773 | 0.562 | 0.03 | | | |
| | 13 | 28.837 | 0.568 | 0.02 | | | |
| | 14 | 28.887 | 0.572 | 0.02 | | | |
| | 15 | 28.928 | 0.574 | 0.02 | | | |
| | … | | | | | | |
| | $\infty$ | 29.189 | | | | | |
| | | | | $j=3/2$ | | | |
| $3s^23p^5\,^2P^o_{1/2}$ | [7s] | | | | | | |
| | 8 | 27.821 | 1.692 | 0.44 | | | |
| | 9 | 28.171 | 1.691 | 0.22 | | | |
| | 10 | 28.401 | 1.690 | 0.13 | | | |
| | 11 | 28.561 | 1.689 | 0.08 | | | |
| | 12 | 28.677 | 1.688 | 0.08 | | | |
| | 13 | 28.764 | 1.688 | 0.04 | | | |
| | 14 | 28.830 | 1.688 | 0.02 | | | |
| | 15 | 28.882 | 1.687 | 0.02 | | | |
| | 16 | 28.923 | 1.687 | 0.02 | | | |
| | … | | | | | | |
| | $\infty$ | 29.189 | | | | | |
| | | | | $j=3/2$ | | | |
| $3s^23p^5\,^2P^o_{1/2}$ | [6d] | | | | 29.615 | 0.732 | 28.9 |
| | 7 | 27.855 | 0.613 | 83.4 | 30.185 | 0.746 | 16.4 |
| | 8 | 28.163 | 0.716 | 25.7 | 30.540 | 0.754 | 10.1 |
| | 9 | 28.395 | 0.720 | 18.1 | 30.775 | 0.759 | 6.6 |
| | 10 | (28.590) | (0.422) | 33.8 | 30.938 | 0.763 | 4.6 |
| | 11 | 28.672 | 0.738 | 3.8 | 31.057 | 0.766 | 3.3 |
| | 12 | 28.760 | 0.745 | 5.3 | 31.145 | 0.767 | 2.5 |
| | 13 | 28.827 | 0.744 | 4.4 | 31.213 | 0.769 | 1.9 |
| | 14 | 28.879 | 0.744 | 3.6 | 31.266 | 0.770 | 1.5 |
| | 15 | 28.921 | 0.744 | 2.9 | 31.308 | 0.771 | 1.2 |
| | … | | | | | | |
| | $\infty$[a] | 29.189 | | | 31.596 | | |

[a]Series limit from NIST Standard Reference Database [42].

TABLE V. Principal quantum numbers $n$, resonance energies (eV), quantum defects $\mu$, and autoionization linewidths [$\Gamma$ (meV)], determined from the QB method for the dominant $3s^2 3p^4(^1D_2)ns,nd$ and $3s^2 3p^4(^1S_0)ns,nd$ series resulting from photoionization of the $3s^2 3p^{5\,2}P^o_{3/2}$ ground state of Ar$^+$.

| Initial state | $n$ | Rydberg series $3s^2 3p^4(^1D_2)ns,nd$ Energy (eV) | $\mu$ | Width ($\Gamma$) $3s^2 3p^4(^1D_2)ns,nd$ Energy (meV) | Rydberg series $3s^2 3p^4(^1S_0)ns,nd$ Energy (eV) | $\mu$ | Width ($\Gamma$) $3s^2 3p^4(^1S_0)ns,nd$ Energy (meV) |
|---|---|---|---|---|---|---|---|
| | | | | $j = 1/2$ | | | |
| $3s^2 3p^{5\,2}P^o_{3/2}$ | [7s] | | | | 29.822 | 1.692 | 1.36 |
| | 8 | 28.007 | 1.673 | 103.4 | 30.387 | 1.691 | 0.39 |
| | 9 | 28.351 | 1.682 | 64.8 | 30.736 | 1.690 | 0.14 |
| | 10 | 28.579 | 1.688 | 43.0 | 30.966 | 1.689 | 0.06 |
| | 11 | 28.739 | 1.692 | 30.0 | 31.126 | 1.689 | 0.03 |
| | 12 | 28.854 | 1.696 | 21.8 | 31.242 | 1.688 | 0.01 |
| | 13 | 28.941 | 1.698 | 16.3 | 31.329 | 1.688 | $< 10^{-2}$ |
| | 14 | 29.007 | 1.700 | 12.5 | 31.395 | 1.688 | $< 10^{-2}$ |
| | 15 | 29.059 | 1.701 | 9.8 | 31.447 | 1.688 | $< 10^{-2}$ |
| | 16 | 29.100 | 1.702 | 7.8 | 31.488 | 1.688 | $< 10^{-2}$ |
| | . . . | | | | | | |
| | $\infty$ | 29.367 | | | 31.774 | | |
| | | | | $j = 1/2$ | | | |
| $3s^2 3p^{5\,2}P^o_{3/2}$ | [6d] | | | | | | |
| | 7 | 28.070 | 0.521 | 0.16 | | | |
| | 8 | 28.389 | 0.540 | 0.11 | | | |
| | 9 | 28.603 | 0.554 | 0.07 | | | |
| | 10 | 28.754 | 0.574 | 0.05 | | | |
| | 11 | 28.869 | 0.546 | 0.04 | | | |
| | 12 | 28.951 | 0.562 | 0.03 | | | |
| | 13 | 29.014 | 0.568 | 0.02 | | | |
| | 14 | 29.065 | 0.572 | 0.02 | | | |
| | 15 | 29.105 | 0.574 | 0.02 | | | |
| | . . . | | | | | | |
| | $\infty$ | 29.367 | | | | | |
| | | | | $j = 3/2$ | | | |
| $3s^2 3p^{5\,2}P^o_{3/2}$ | [7s] | | | | | | |
| | 8 | 27.999 | 1.692 | 0.44 | | | |
| | 9 | 28.348 | 1.691 | 0.26 | | | |
| | 10 | 28.579 | 1.690 | 0.13 | | | |
| | 11 | 28.739 | 1.689 | 0.08 | | | |
| | 12 | 28.855 | 1.688 | 0.06 | | | |
| | 13 | 28.941 | 1.688 | 0.04 | | | |
| | 14 | 29.098 | 1.688 | 0.03 | | | |
| | 15 | 29.060 | 1.687 | 0.02 | | | |
| | 16 | 29.101 | 1.687 | 0.02 | | | |
| | . . . | | | | | | |
| | $\infty$ | 29.367 | | | | | |
| | | | | $j = 3/2$ | | | |
| $3s^2 3p^{5\,2}P^o_{3/2}$ | [6d] | | | | 29.793 | 0.732 | 28.9 |
| | 7 | 28.033 | 0.613 | 83.4 | 30.363 | 0.746 | 16.4 |
| | 8 | 28.341 | 0.716 | 25.7 | 30.718 | 0.754 | 10.1 |
| | 9 | 28.573 | 0.720 | 18.1 | 30.953 | 0.759 | 6.6 |
| | 10 | (28.774) | (0.422) | 33.8 | 31.116 | 0.763 | 4.6 |
| | 11 | 28.850 | 0.738 | 3.8 | 31.234 | 0.766 | 3.3 |
| | 12 | 28.937 | 0.745 | 5.3 | 31.322 | 0.768 | 2.5 |
| | 13 | 29.004 | 0.744 | 4.4 | 31.390 | 0.769 | 1.9 |
| | 14 | 29.047 | 0.744 | 3.6 | 31.443 | 0.770 | 1.5 |
| | 15 | 29.099 | 0.744 | 2.9 | 31.485 | 0.771 | 1.2 |
| | . . . | | | | | | |
| | $\infty$[a] | 29.367 | | | 31.774 | | |

[a]Series limit from NIST Standard Reference Database [42].

TABLE VI. Principal quantum numbers $n$, resonance energies (eV), quantum defects $\mu$, and autoionization linewidths [$\Gamma$ (meV)], determined from the QB method for the dominant $3s^2 3p^4(^1D_2)ns,nd$ and $3s^2 3p^4(^1S_0)nd$ series resulting from photoionization of the $3s^2 3p^5\,^2P^o_{3/2}$ ground state of $Ar^+$.

| Initial state | $n$ | Rydberg series $3s^2 3p^4(^1D_2)ns,nd$ Energy (eV) | $\mu$ | Width ($\Gamma$) $3s^2 3p^4(^1D_2)ns,nd$ Energy(meV) | Rydberg series $3s^2 3p^4(^1S_0)nd$ Energy (eV) | $\mu$ | Width ($\Gamma$) $3s^2 3p^4(^1S_0)nd$ Energy (meV) |
|---|---|---|---|---|---|---|---|
| | | $j = 5/2$ | | | | | |
| $3s^2 3p^5\,^2P^o_{3/2}$ | [7s] | | | | | | |
| | 8 | 27.999 | 1.692 | 0.27 | | | |
| | 9 | 28.348 | 1.691 | 0.12 | | | |
| | 10 | 28.579 | 1.690 | 0.07 | | | |
| | 11 | 28.739 | 1.689 | 0.04 | | | |
| | 12 | 28.855 | 1.688 | 0.03 | | | |
| | 13 | 28.941 | 1.688 | 0.02 | | | |
| | 14 | 29.008 | 1.688 | 0.01 | | | |
| | 15 | 29.060 | 1.687 | $< 10^{-2}$ | | | |
| | 16 | 29.101 | 1.687 | $< 10^{-2}$ | | | |
| | ... | | | | | | |
| | $\infty$ | 29.367 | | | | | |
| | | $j = 5/2$ | | | | | |
| $3s^2 3p^5\,^2P^o_{3/2}$ | [6d] | | | | 29.790 | 0.735 | 25.2 |
| | 7 | 27.983 | 0.729 | 2.25 | 30.361 | 0.749 | 14.3 |
| | 8 | 28.335 | 0.737 | 1.40 | 30.717 | 0.757 | 8.8 |
| | 9 | 28.569 | 0.742 | 0.94 | 30.952 | 0.763 | 5.8 |
| | 10 | 28.731 | 0.745 | 0.66 | 31.116 | 0.766 | 4.0 |
| | 11 | 28.849 | 0.748 | 0.40 | 31.234 | 0.769 | 2.9 |
| | 12 | 28.937 | 0.750 | 0.33 | 31.322 | 0.771 | 2.2 |
| | 13 | 29.004 | 0.751 | 0.26 | 31.390 | 0.773 | 1.7 |
| | 14 | 29.057 | 0.752 | 0.20 | 31.443 | 0.774 | 1.3 |
| | 15 | 29.099 | 0.753 | 0.16 | 31.485 | 0.775 | 1.0 |
| | ... | | | | | | |
| | $\infty$[a] | 29.367 | | | 31.774 | | |

[a]Series limit from NIST Standard Reference Database [42].

quantum defect $\mu$ and the resonance autoionizing linewidth $\Gamma$ (meV) of the first few members of the dominant Rydberg series originating from the $^2P^o_{1/2}$ metastable and the $^2P^o_{3/2}$ ground state of the $Ar^+$ ion are listed in the Tables IV–VI. The results for the appropriate resonance parameters for the dominant Rydberg resonance series found in the spectra of the PI cross section for the ground and metastable states of $Ar^+$, lying below the $^1D_2$ and $^1S_0$ thresholds of the product $Ar^{2+}$ ion are listed in Tables IV–VI. As may be seen from the results of the QB analysis, many members of the various Rydberg series have resonance linewidths smaller than the experimental photon bandwidth of 10 meV, therefore making their detection extremely difficult. Finally we note that interloping resonances $3s^2 3p^4(^1S_0)6s,5d$ are present in the spectrum below the $3s^2 3p^4(^1D_2)$ threshold (as clearly illustrated in Figs. 6 and 9) disrupting the regular pattern of the Rydberg series.

## V. SUMMARY

Absolute photoionization cross sections have been measured for a statistical mixture of ground-state and metastable $Ar^+$ in the photon energy range $\approx$27–60 eV with a nominal energy resolution of 10 meV. The cross section in this energy region is characterized by a wealth of resonance features due to indirect photoionization. The dominant features were spectroscopically assigned to Rydberg series, and quantum defects were determined. A conservative estimate for the accuracy of the resonance energies is $\pm$10 meV. The natural linewidths were determined from the $R$-matrix method which we would estimate to be accurate to 10%. Over the entire energy range investigated, the theoretical results for the photoionization cross sections on this Cl-like system obtained from an intermediate-coupling Breit-Pauli $R$-matrix approach are in excellent agreement with the high-resolution measurements. The main thrust of this joint investigation is the coupling of high experimental sensitivity and photon energy resolving power with state-of-the-art theoretical predictions. The excellent agreement between theory and experiment over the entire energy range gives added confidence in both results. The photoionization cross sections from the present study on this Cl-like ion are suitable for inclusion in state-of-the-art photoionization modeling codes such as CLOUDY [34,35] and XSTAR [36], which are used to numerically simulate the thermal and ionization structure of ionized astrophysical nebulae.

## ACKNOWLEDGMENTS

[1] J. N. Bregman and J. P. Harrington, Astrophys. J. **309**, 833 (1986).

[2] I. Hofmann, Laser Part. Beams **8**, 527 (1990).

[3] W. Cunto, C. Mendoza, F. Ochsenbein, and C. J. Zeippen, Astron. Astrophys. **275**, L5 (1993).

[4] C. A. Iglesias and F. J. Rogers, Astrophys. J. **464**, 943 (1996).

[5] M. A. Bautista and T. R. Kallman, Astrophys. J. Suppl. Ser. **134**, 139 (2001).

[6] K. Cunha, I. Hubeny, and T. Lanz, Astrophys. J. **647**, L143 (2006).

[7] C. Esteban, M. Peimbert, J. García-Rojas, M. Ruiz, A. Peimbert, and M. Rodríguez, Mon. Not. R. Astron. Soc. **355**, 229 (2004).

[8] J. S. Kaastra, C. P. de Vries, E. Constantini, and J. W. A. den Herder, Prog. Theo. Phys. **169**, 204 (2007).

[9] T. Lanz, K. Cunha, J. Holtzman, and I. Hubeny, Astrophys. J. **678**, 1342 (2008).

[10] A. M. Covington et al., Phys. Rev. A **66**, 062710 (2002).

[11] A. Aguilar et al., J. Phys. B **38**, 343 (2005).

[12] U. Fano and J. W. Cooper, Phys. Rev. **137**, 1364 (1965).

[13] H. Kjeldsen, J. Phys. B **39**, R325 (2006).

[14] J. B. West, J. Phys. B **34**, R45 (2001).

[15] I. C. Lyon, B. Peart, J. B. West, and K. Dolder, J. Phys. B **19**, 4137 (1986).

[16] R. A. Phaneuf, C. C. Havener, G. H. Dunn, and A. Müller, Rep. Prog. Phys. **62**, 1143 (1999).

[17] H. Kjeldsen, F. Folkmann, H. Knudsen, M. S. Rasmusssen, J. B. West, and T. Andersen, Astrophys. J. **524**, L143 (1999).

[18] A. M. Covington et al., Phys. Rev. Lett. **87**, 243002 (2001).

[19] H. Kjeldsen, B. Kristensen, R. L. Brooks, F. Folkmann, H. Knudsen, and T. Andersen, Astrophys. J. Suppl. Ser. **138**, 219 (2002).

[20] A. Müller, R. A. Phaneuf, A. Aguilar, M. F. Gharaibeh, A. S. Schlachter, I. Álvarez, C. Cisneros, G. Hinojosa, and B. M. McLaughlin, J. Phys. B **35**, L137 (2002).

[21] A. Müller et al., J. Phys. B **42**, 235602 (2009).

[22] A. Müller, S. Schippers, R. A. Phaneuf, A. L. D. Kilcoyne, H. Bräuning, A. S. Schlachter, M. Lu, and B. M. McLaughlin, J. Phys. B **43**, 225201 (2010).

[23] N. Beverini, G. del Gobbo, G. L. Genovesi, F. Maccarrone, F. Strumia, F. Paganucci, A. Turco, and M. Andrenucci, IEEE J. Quantum Electron. **332**, 1874 (1996).

[24] N. C. M. Fuller, I. P. Herman, and V. M. Donnelly, J. Appl. Phys. **90**, 3182 (2001).

[25] S-C. Park and Y-B. Park, J. Elect. Mat. **37**, 1565 (2008).

[26] G. A. Alna'washi, M. Lu, M. Habibi, R. A. Phaneuf, A. L. D. Kilcoyne, A. S. Schlachter, C. Cisneros, and B. M. McLaughlin, Phys. Rev. A **81**, 053416 (2010).

[27] S. W. J. Scully et al., J. Phys. B **39**, 3957 (2006).

[28] S. W. J. Scully et al., J. Phys. Conf. Ser. **58**, 387 (2007).

[29] A. Müller, S. Schippers, R. A. Phaneuf, S. W. J. Scully, A. Aguilar, C. Cisneros, M. F. Gharaibeh, A. S. Schlachter, and B. M. McLaughlin, J. Phys. B **43**, 135602 (2010).

[30] A. Müller, R. A. Phaneuf, A. Aguilar, M. F. Gharaibeh, A. S. Schlachter, I. Álvarez, C. Cisneros, G. Hinojosa and B. M. McLaughlin, Nucl. Instrum. Methods Phys. Res. Sect. B **205**, 301 (2003).

[31] S. Schippers, A. Müller, B. M. McLaughlin, A. Aguilar, C. Cisneros, E. D. Emmons, M. F. Gharaibeh, and R. A. Phaneuf, J. Phys. B **36**, 3371 (2003).

[32] A. Müller, S. Schippers, R. A. Phaneuf, A. L. D. Kilcoyne, H. Bräuning, A. S. Schlachter, M. Lu, and B. M. McLaughlin, J. Phys. Conf. Ser. **58**, L383 (2007).

[33] A. S. Schlachter et al., J. Phys. B **37**, L103 (2004).

[34] G. J. Ferland, K. T. Korista, D. A. Verner, J. W. Ferguson, J. B. Kingdon, and E. M. Verner, Publ. Astron. Soc. Pac. **110**, 761 (1998).

[35] G. J. Ferland, Annu. Rev. Astron. Astrophys. **41**, 517 (2003).

[36] T. R. Kallman and M. A. Bautista, Astrophys. J. Suppl. Ser. **134**, 139 (2001).

[37] P. G. Burke and W. D. Robb, in Advances in Atomic and Molecular Physics, edited by D. R. Bates and B. Bederson, Vol. 11 (Academic, New York, 1975), p. 143.

[38] C. P. Ballance and D. C. Griffin, J. Phys. B **39**, 3617 (2006).

[39] P. G. Burke and K. A. Berrington, Atomic and Molecular Processes: An R-matrix Approach (IOP Publishing, Bristol, UK, 1993).

[40] K. A. Berrington, W. Eissner, and P. H. Norrington, Comput. Phys. Commun. **92**, 290 (1995).

[41] F. Robicheaux, T. W. Gorczyca, M. S. Pindzola, and N. R. Badnell, Phys. Rev. A **52**, 1319 (1995).

[42] Y. Ralchenko, A. E. Kramida, J. Reader, and NIST ASD Team, NIST Atomic Spectra Database (version 4.0.1), National Institute of Standards and Technology, Gaithersburg, MD, 2010 [http://physics.nist.gov/asd].

[43] J. E. Hansen and W. Persson, J. Phys. B **20**, 693 (1987).

[44] L. Quigley and K. A. Berrington, J. Phys. B **29**, 4529 (1996).

[45] L. Quigley, K. A. Berrington, and J. Pelan, Comput. Phys. Commun. **114**, 225 (1998).

[46] C. P. Ballance, K. A. Berrington, and B. M. McLaughlin, Phys. Rev. A **60**, R4217 (1999).